
**MULTI-DIRECTIONAL
SCATTERING MODELS
FOR 3D ULTRASOUND**

U. Z. Ijaz, R. J. Housden, G. M. Treece
R. W. Prager, and A. H. Gee

CUED/F-INFENG/TR 661

January 2011

University of Cambridge
Department of Engineering
Trumpington Street
Cambridge CB2 1PZ
United Kingdom

Email: uzi20/rjh80/gmt11/rwp/ahg @eng.cam.ac.uk

Multi-directional scattering models for 3D ultrasound

Umer Zeeshan Ijaz, R. James Housden, Graham M. Treece, Richard W. Prager,
and Andrew H. Gee

University of Cambridge
Department of Engineering
Trumpington Street
Cambridge CB2 1PZ

Abstract

An ultrasound image is created from back-scattered echoes originating both from diffuse and directional scattering. It is potentially useful to separate these two components for the purpose of tissue characterization. This paper presents several models for visualization of scattering fields in 3D ultrasound. By scanning the same anatomy from multiple directions, we can observe the variation of specular intensity as a function of viewing angle. This paper considers two models for estimating the diffuse and specular components of the backscattered intensity: a modification of the well-known Phong reflection model and an existing exponential model. We examine 2D implementations and also propose novel 3D extensions of these models in which the probe is not constrained to rotate within a plane. Both simulation and experimental results show that improved performance can be achieved with 3D models.

1 Introduction

In ultrasonic imaging, the insonified beam is scattered in different directions given the spatial location and orientation of tissues and boundaries. Backscattering happens as a result of non-uniformity of the medium in the direction of insonification and also depends on other factors such as the size of the scatterers, their geometric arrangement, and the differences in density and compressibility of the scatterers and surrounding medium. The theme of this paper is characterization of tissue regions based on their scattering properties, particularly in the identification of regions with high directional scattering. This type of tissue characterization may be useful clinically [1].

Some success has already been reported in the literature on tissue characterization, though most of it focuses on diffuse scattering. For example, a procedure for separating the diffuse from the specular scattering based on second-order statistics is presented in [2]. Similarly, in [3], it is assumed that fully-developed speckle (a type of diffuse scattering) follows a Rayleigh distribution and a Kolmogorov-Smirnov goodness of fit test is used to differentiate between Rayleigh and non-Rayleigh regions. In [4], the reflected ultrasound beam is modelled as a superposition of diffuse, specular and quasiperiodic structures by employing harmonic models for particle movements. This method gives two types of diffuse image: a diffuse friction coefficient image and a diffuse forced frequency image with the latter showing a better contrast between tissues.

Recently, multi-directional ultrasound echo signals have been considered for differentiation and characterization of specular reflection [1]. In this work, the authors have utilised limited-angle spatial compound imaging at each point of the image plane as a function of angle of insonification. A symmetrical 2D exponential model is fitted in terms of least squares to the measured backscatter over different angles of insonification. The above procedure has promising prospects for differentiation of scar tissues from the surroundings based on the specular reflections. In this paper, we are extending this work to consider an alternative reflection model. Our motivation for this research comes from the Phong reflection model [5] that has become the *de facto* standard as an illumination model in computer graphics applications. This model is an empirical model and considers that the specular reflection is stronger in one direction and falls off rapidly as we move away from it. This approach has the advantage of being conceptually simple and in a different

context [6] has previously been used as a reflection model for deconvolution of a single 2D ultrasound image. Their approach estimates the specular direction using an edge detection approach from the image data. In comparison, we use multiple scans from different directions to determine the true reflection properties of the underlying tissue. Since scattering is inherently 3D, we also extend the models to allow for variations in three dimensions.

2 Methods

2.1 2D Multi-directional Scattering Models

Given a set of image intensity values for the same location recorded with different directions of insonification, the diffuse and specular back-scatter properties at that location can be separated. We modify the conventional Phong model and assume the reflectance to be the sum of two terms

$$b^{(k)} = d + t|\cos(\phi^{(k)} - \theta)|^n \quad (1)$$

where $b^{(k)}$ is the observed intensity in the k^{th} direction, d is the diffuse component which is independent of insonification direction and $t|\cos(\phi^{(k)} - \theta)|^n$ is the specular component which is a function of the angle between the direction of insonification $\phi^{(k)}$ and the true specular direction of the tissue θ . Furthermore, n defines how quickly the specular component decreases with angle. This 2D formulation assumes that angular variations are within a plane. The model takes the absolute value of the cosine to avoid complex solutions produced by negative values of the cosine combined with fractional values of n . For comparative purposes, we will use the symmetrical exponential model proposed in [1] in which a Gaussian function is used to model the specular variation

$$b^{(k)} = d + te^{-n(\phi^{(k)} - \theta)^2} \quad (2)$$

where n in this case controls the width of the Gaussian and so again defines how quickly the specular component decreases with angle. In the above equations, only $b^{(k)}$, $\phi^{(k)}$ are known *a priori* and we are interested in estimating the rest of the parameters: d , t , n , and θ .

2.2 3D Multi-directional Scattering Models

These above models are inherently 2D but it is possible to record 3D data by acquiring multiple volumes from different directions, e.g. using a mechanically-swept 3D probe. In this paper, we look at just a single slice of data (generated using the reslicing algorithm in [7]) through the 3D volumes.

We can also apply the following 3D versions of the models. We define the rotation matrices about the z and x axes as:

$$\mathbf{R}_z = \begin{bmatrix} \cos \theta & \sin \theta & 0 \\ -\sin \theta & \cos \theta & 0 \\ 0 & 0 & 1 \end{bmatrix}, \mathbf{R}_x = \begin{bmatrix} 1 & 0 & 0 \\ 0 & \cos \Psi & \sin \Psi \\ 0 & -\sin \Psi & \cos \Psi \end{bmatrix} \quad (3)$$

where, for the ultrasound probe, rotation about the z-axis is lateral tilt and rotation about the x-axis is elevational tilt. The combination of the two is defined as

$$\mathbf{R}_x \mathbf{R}_z = \begin{bmatrix} \cos \theta & \sin \theta & 0 \\ -\sin \theta \cos \Psi & \cos \theta \cos \Psi & \sin \Psi \\ \sin \theta \sin \Psi & -\cos \theta \sin \Psi & \cos \Psi \end{bmatrix} \quad (4)$$

where the direction of scattering is given relative to the y direction, i.e. by the second column of the matrix in the above equation. Let \vec{v} be the unit directional vector for the direction of

insonification. The 3D Phong model then becomes

$$b^{(k)} = d + t \left| \begin{bmatrix} \sin \theta \\ \cos \theta \cos \Psi \\ -\cos \theta \sin \Psi \end{bmatrix} \cdot \begin{bmatrix} \vec{v}_x^{(k)} \\ \vec{v}_y^{(k)} \\ \vec{v}_z^{(k)} \end{bmatrix} \right|^n \quad (5)$$

where Ψ is an additional parameter for the 3D model. In a similar manner, we can extend the symmetrical exponential model of [1] to 3D as

$$b^{(k)} = d + te^{-n \left(\cos^{-1} \left| \begin{bmatrix} \sin \theta \\ \cos \theta \cos \Psi \\ -\cos \theta \sin \Psi \end{bmatrix} \cdot \begin{bmatrix} \vec{v}_x^{(k)} \\ \vec{v}_y^{(k)} \\ \vec{v}_z^{(k)} \end{bmatrix} \right| \right)^2} \quad (6)$$

where the inverse cosine gives the absolute difference in angles as in the original 2D equation.

2.3 Estimation model

The procedure for estimation of the scattering fields in 3D data is:

Step 1 Acquire multiple volumes of the target from different directions of insonification.

Step 2 Fit an $M \times N$ reslice plane around the acquired P volumes at an arbitrary orientation with the direction vectors for the reslice plane given by the orthogonal unit vectors \vec{e}_x , \vec{e}_y , and \vec{e}_z , where \vec{e}_z is normal to the plane. This reslice is large enough to contain the maximum extent of all the volumes.

Step 3 **for** each volume, $k = 1$ to P

- Obtain the $M \times N$ reslice image, $b^{(k)}$, using only the frames in the current volume, and corresponding $M \times N$ array of direction vectors, $\vec{v}^{(k)}$.
- Apply a Gaussian smoothing filter to the reslice image, $b^{(k)}$. The purpose of the smoothing filter is to reduce the noise in the images.

Step 4 **for** each pixel, $i = 1$ to M , and $j = 1$ to N

– **if** 2D model **then**

* **for** $k = 1$ to P

- Project the direction of insonification vector at each pixel, $\vec{v}^{(ijk)}$, into the reslice plane: $\vec{u}^{(ijk)} = \vec{v}^{(ijk)} - (\vec{v}^{(ijk)} \cdot \vec{e}_z) \vec{e}_z$.
- Obtain the projected angle of insonification in the reslice plane relative to \vec{e}_y , the y -direction of the reslice: $\phi^{(ijk)} = \sin^{-1}((\vec{u}^{(ijk)} \times \vec{e}_y) \cdot \vec{e}_z)$.

– **if** sufficient angles image the current pixel **then** solve the box-constraint Levenberg-Marquardt problem [8]:

* **if** 2D model **then**

- Solve for $d^{(ij)}$, $t^{(ij)}$, $\theta^{(ij)}$, and $n^{(ij)}$ using either of the 2D models given in Eqs. (1,2). For the reasons given in Fig. 1, n can alternatively be fixed and we only solve for the remaining three parameters.

* **if** 3D model **then**

- Solve for $d^{(ij)}$, $t^{(ij)}$, $\theta^{(ij)}$, $\Psi^{(ij)}$ and $n^{(ij)}$ using either of the 3D models given in Eqs. (5,6). Alternatively, n can be fixed and we only solve for the remaining four parameters.

Step 5 Output

– **if** 2D model **then**

- * Display the diffuse back-scatter component, \hat{d} , specular scattering strength, \hat{t} , and specular scattering field $[\hat{t} \cos \hat{\theta}, \hat{t} \sin \hat{\theta}]^T$.

– if 3D model then

* Display the diffuse back-scatter component, \hat{d} , specular scattering strength, \hat{t} , and specular scattering field $[\hat{t}\hat{f}\cdot\vec{e}_x, \hat{t}\hat{f}\cdot\vec{e}_y]^T$ where $\hat{f} = [\sin\hat{\theta}, \cos\hat{\theta}\cos\hat{\Psi}, -\cos\hat{\theta}\sin\hat{\Psi}]^T$.

In all the experiments in this paper, we preprocessed the images with a 5×5 Gaussian smoothing filter with a standard deviation of 5 pixels. In step 5, the maximum number of iterations in the Levenberg-Marquardt Method was set to 1000. The iterative solution is initialised as follows:

$$d_0 = \text{avg}(b^{(k)}) \quad (7)$$

$$t_0 = \max(b^{(k)}) - d_0 \quad (8)$$

for exponential model:

$$n_0 = 0.031 \quad (9)$$

for Phong model:

$$n_0 = 200 \quad (10)$$

for 2D:

$$\theta_0 = \arg \max_{\phi^{(k)}}(b^{(k)}) \quad (11)$$

for 3D:

$$m = \arg \max_k(b^{(k)}) \quad (12)$$

$$\theta_0 = \sin^{-1}(\vec{v}_x^{(m)}) \quad (12)$$

$$\Psi_0 = \cos^{-1}(\vec{v}_y^{(m)} / \cos(\theta_0)) \quad (13)$$

Here, the value of n is initialised differently depending on which model we use. Also, the specular direction is initialised to the direction of insonification with maximum back-scatter $\vec{v}^{(m)}$. We have constrained the optimisation as follows: $d \geq 0$, $t \geq 0$, $n \geq 0$, $-\pi \leq \theta \leq \pi$, and $-\pi \leq \Psi \leq \pi$. Only positive values of d and t are allowed because we want to avoid those situations in which either of d or t becomes very large while the other becomes negative.

2.4 Field II Simulations

The simulated data were generated using Field II [9], which was set up to model a typical ultrasound transducer with centre frequency 6.5 MHz. Each RF frame comprised 127 A-lines at a pitch of 0.3 mm, giving a lateral B-scan width of 38.1 mm. Each A-line was sampled at 66.67 MHz to a depth of 46.2 mm. Both the lateral and elevational focal depths were set to 20 mm. A random distribution of scatterers at a density of $15 / \text{mm}^3$ and normally distributed scattering strengths provided a diffuse scattering component. In addition, various patterns of regularly arranged scatterers of equal scattering strength were used to produce a specular scattering effect. We created three simulated datasets for the experiments in this paper. First, in order to characterise the variation of specular intensity with viewing angle, we produced a dataset comprising only specular scattering with no randomly distributed scatterers. The scatterers were placed evenly spaced in straight lines at three depths: 7 mm, 20 mm (the focal depth) and 33 mm. We created 91 separate images with the lines rotated by 0 degrees up to 90 degrees to the viewing direction about their centres, changing in steps of 1 degree (shown in Fig. 1(a)). We also experimented with different scatterer densities along the lines by creating images for spacings of 1, 2, 3, 4, 5, 10, 20, 30, 40, 50, 60, 70, 80, 90 and 100 microns. The purpose of this simulation was to confirm that the models are appropriate and to calibrate for the value of n .

Second, we combined specular and diffuse scatterers together in 2D datasets. With 1D lines of specular scatterers and a scatterer spacing of 4 microns, we found that a scattering strength ratio of 1 to 2 (equal specular scattering strength to standard deviation of diffuse scattering strength) produced a typical ultrasound image. In the first dataset, the specular scatterers were arranged in five horizontal lines at different depths (10, 15, 20, 25 and 30 mm) and of length 10 mm. Rather than rotating the lines about their centres, for this dataset we simulated the probe tilting in plane about the lateral centre of the image at the focal depth. The dataset (shown in Fig. 2(a,b)) comprised 31 images, at angles of -15 to $+15$ degrees to the vertical, changing in steps of 1 degree. This dataset tests the algorithms with specular scattering at various depths. In the second dataset (shown in Fig. 3(a,b)) we produced an arc of diameter 5 cm and imaged it in the same manner as before, i.e. at angles of -15 to $+15$ degree. This dataset

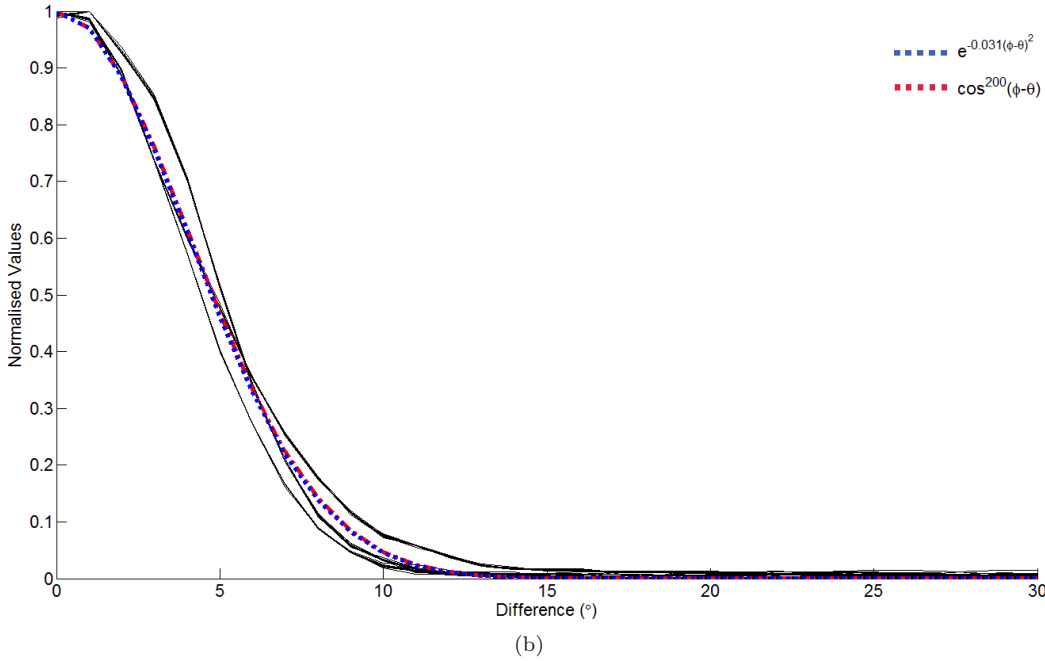
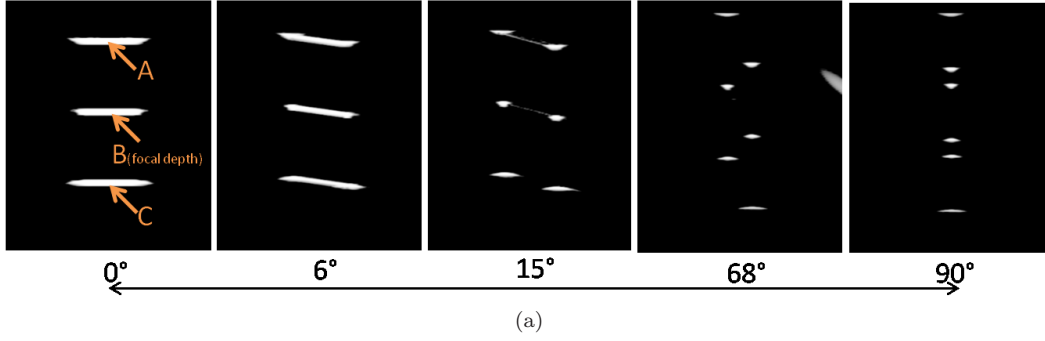


Figure 1: **Specular variation with angle.** (a) Sample images with a 0 to 90 degree range of insonification angle and 4 micron scatterer spacing. The points A, B, and C indicate where we measured the specular intensity in each line. The measurement points are at the centre of each line. (b) Plots of all combinations of 3 line depths and 15 scatterer spacings giving 45 separate plots. Each plot was normalized by its maximum value at angle zero. The angular variation is approximated by a plot of the cosine function, $\cos(\phi - \theta)^{200}$, shown in red, and by a Gaussian function, $e^{-0.031(\phi-\theta)^2}$, shown in blue.

demonstrates the performance of the algorithms when the specular direction varies within the image. The entire simulated movement in both cases was within a single plane, in order to assess the technique in 2D.

Finally, in order to test the 3D version of the technique, we simulated a 3D dataset containing both diffuse scatterers and a single 2D lateral-elevational patch of specular scatterers. The specular scatterer spacing was 4 microns in each of the two directions. The patch was 5 mm \times 5 mm and was at the focal depth. The scattering strength ratio was increased to 1 to 700, because the 2D patch had a much higher density of specular scatterers than the 1D lines used previously. The dataset comprised 17 volumes of data, each of 25 frames at 0.3 mm spacing, giving volumes covering 7.2 mm elevationally. One volume was vertical, 8 were tilted laterally at $\pm(2.5, 5.0, 7.5, 10.0)$ degrees and 8 were tilted elevationally at the same angles. The complete dataset is shown in Figs. 4 and 5.

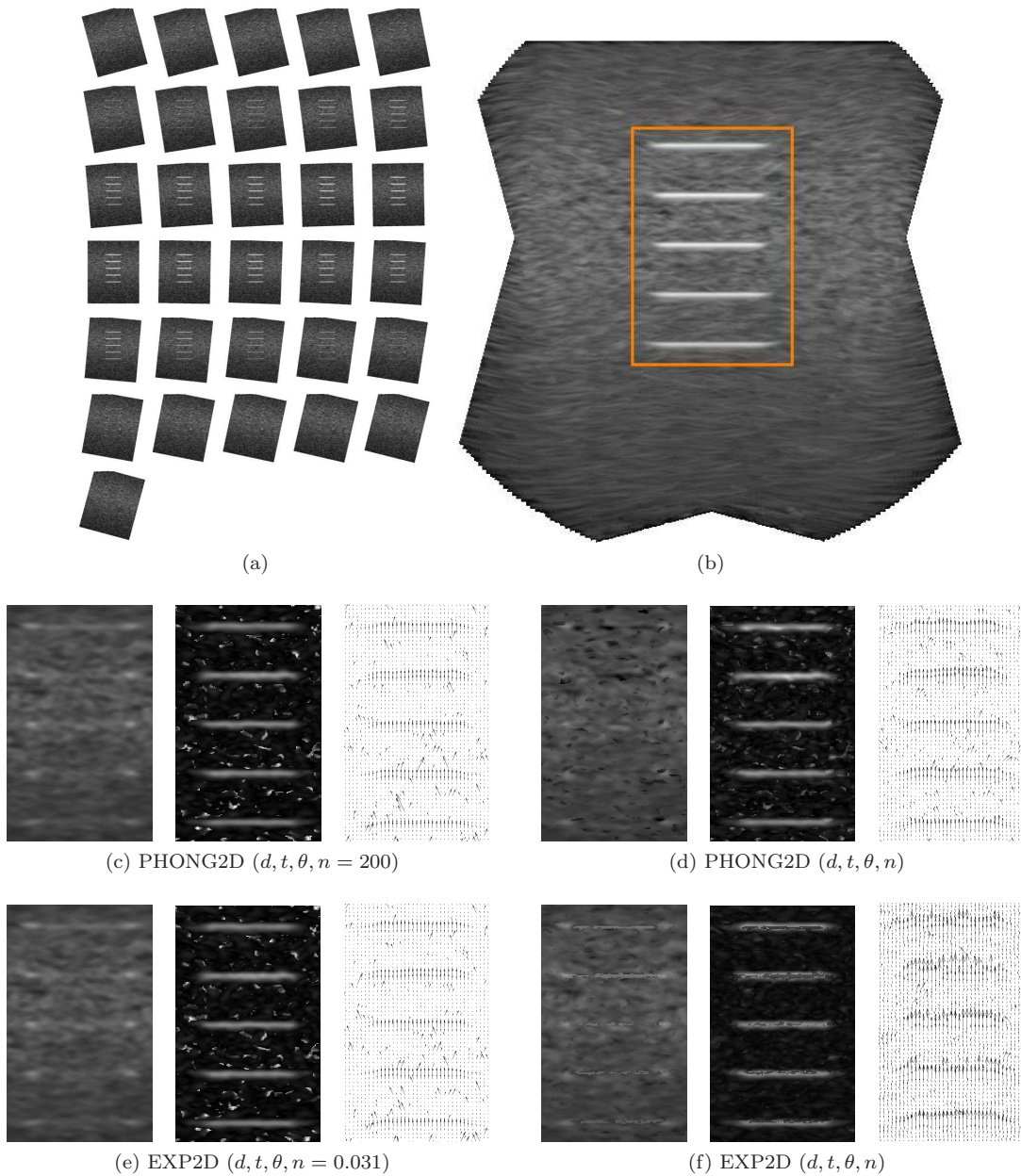


Figure 2: **Scatter field results for 2D simulated lines data.** (a) The 31 individual B-mode images. (b) The maximum compounded B-mode image formed from the individual images. (c-f) From left to right: estimated diffuse back-scatter component d , estimated specular scattering strength t and estimated magnitude and direction of specular scattering. (c) and (e) estimate three parameters, (d) and (f) estimate four.

2.5 *In Vitro* Experiments

We recorded *in vitro* ultrasound data using a GE RSP6-12 (GE Healthcare, Chalfont St. Giles, UK) mechanically-swept 3D probe interfaced to a Dynamic Imaging Diasus US machine. The 3D probe had a centre frequency of 7.5 MHz with a footprint of approximately 5 cm laterally by 5.5 cm elevationally. The depth setting was 3 cm with a single lateral focus at 1.5 cm. The analogue RF echo signals were then converted to B-scan images by the Stradwin software [10, 11] (Medical Imaging Group, University of Cambridge, Cambridge, UK). For these experiments, each B-scan's position and orientation was recorded

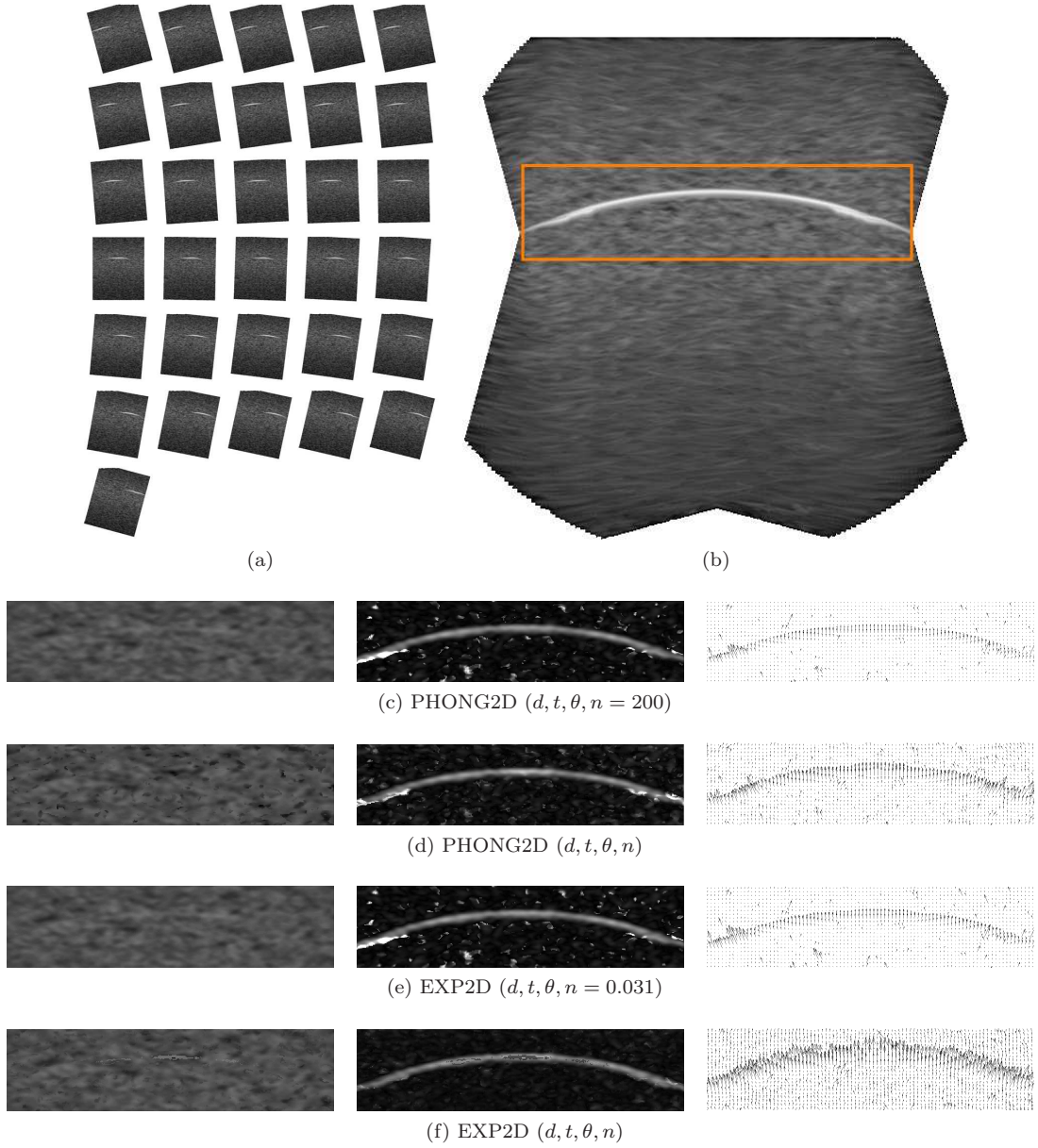


Figure 3: **Scatter field results for 2D simulated arc data.** See the caption to Fig. 2 for an explanation of the subfigures.

using a Northern Digital Polaris optical tracking system [12] (Northern Digital Inc., Waterloo, Ontario, Canada) with calibration performed according to [13]. We recorded 7 volumes each of 50 frames sweeping out an angle of 10 degrees. The average frame spacing was 0.34 mm. The frame size was 250×352 pixels with a pixel size of 0.1 mm/pixel.

The scanning subject was a speckle phantom (see Fig. 6(a)) consisting of an agar cylinder of 5 cm length and 6 cm diameter, with a uniform distribution of aluminium oxide powder providing scattering. Two cuts were made along the curved edge, one to provide a flat base to the phantom and one to allow a reflective specular scattering surface to be inserted. The reflective material was a thin sheet of aluminium foil, which provided a strong specular image inside the diffusely scattering agar phantom. A layer of ultrasound coupling gel was added to both sides of the foil to minimise signal loss across the foil.

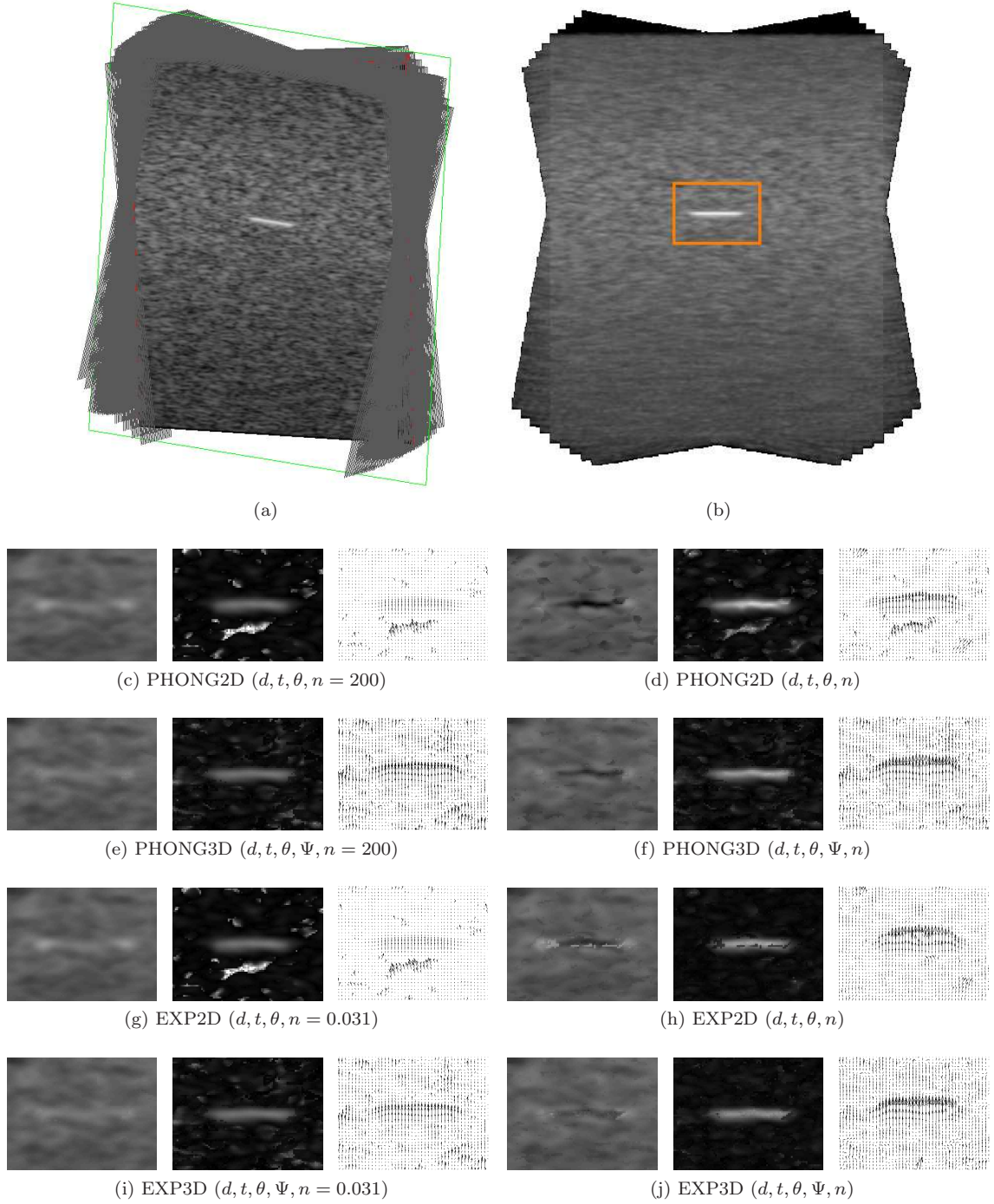


Figure 4: **3D simulated data results with axial-lateral reslice.** (a) 3D view of the 17 volumes showing the location of the reslice plane. (b) A blended view of the reslices from the individual volumes with the region of interest highlighted with an outline. (c-j) From left to right: estimated diffuse back-scatter component d , estimated specular scattering strength t and estimated magnitude and direction of specular scattering.

3 Results and Discussion

The variation of specular intensity with angle is shown in Fig. 1. It can be seen that both models closely match the reduction of back-scattered intensity with angle. After normalising the angular intensity

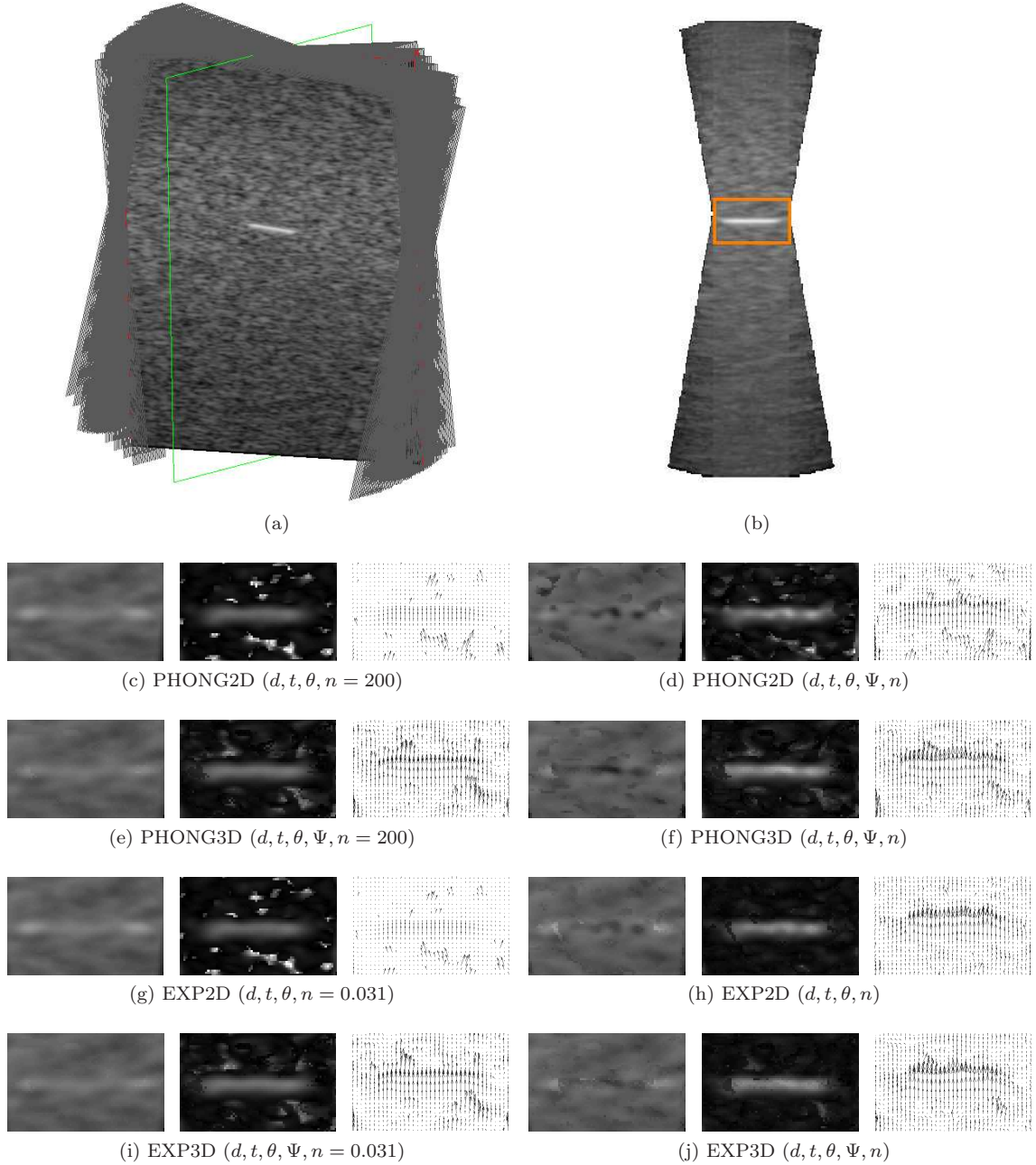


Figure 5: **3D simulated data results with axial-elevational reslice.** See the caption to Fig. 4 for an explanation of the subfigures.

variation to the maximum at zero degrees, we found that a value of $n = 200$ for the Phong model, and $n = 0.031$ for the exponential model, gives the best approximation to the actual variation in all cases. Using these calibrated values of n , we applied the 2D model to our simulated 2D datasets. For each model, we considered two cases: fixing n at the calibrated value, and solving for n as an additional parameter but initialised to its calibrated value. The results are shown in Figs. 2 and 3. In all cases, there is a clear separation of diffuse and specular components and all the specular directions are correctly angled perpendicular to the specular features. However, there are some differences between the four approaches. First, there are noticeable errors in the background regions of the specular strength image t when n is fixed. We believe that this happens because the optimisation is unconstrained beyond the range of measured

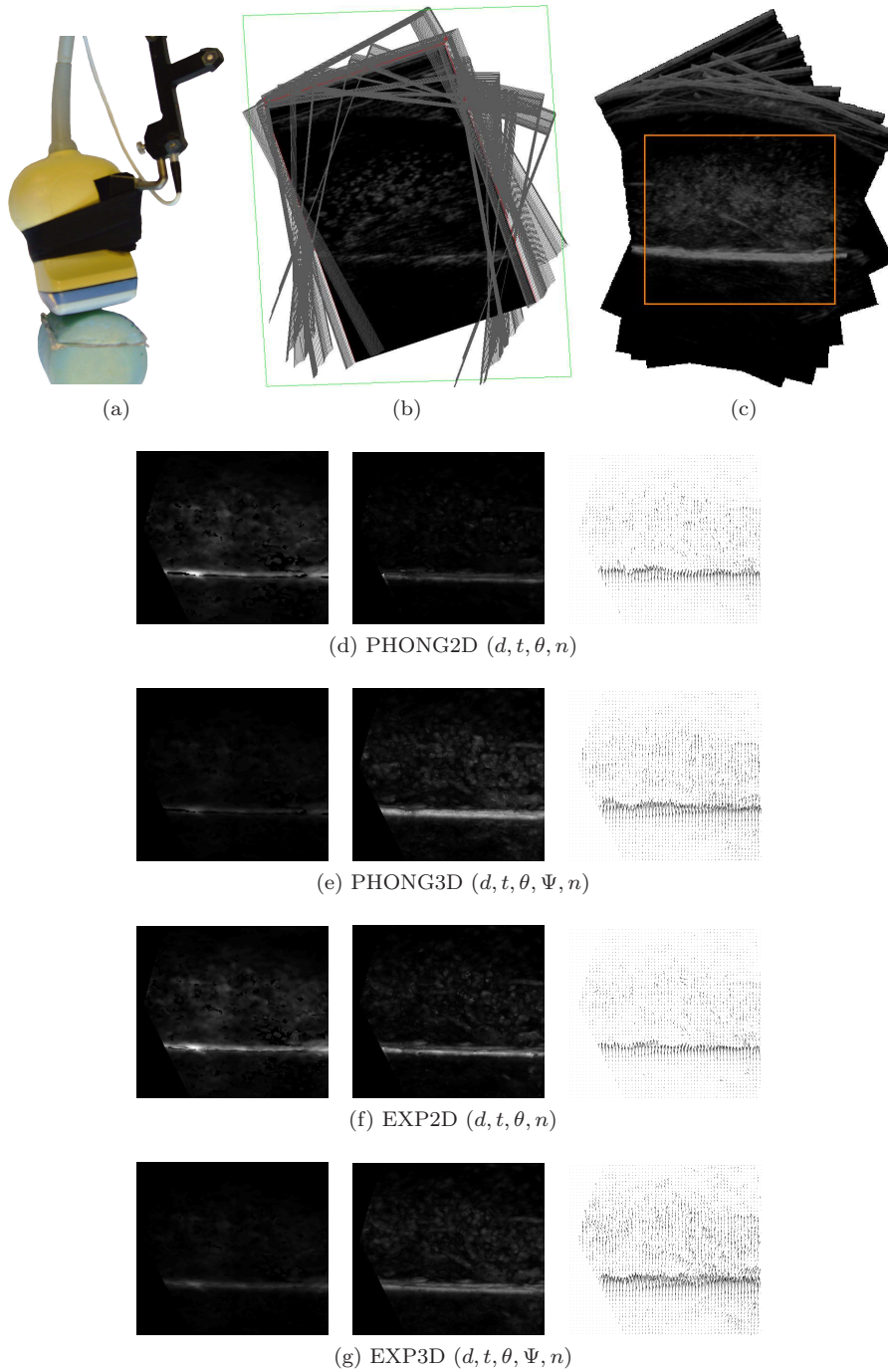


Figure 6: **3D experimental data results.** (a) The experimental setup, showing a GE RSP6-12 3D probe with Northern Digital Polaris optical tracker scanning a phantom. The elevational direction of the probe is out of the page and the probe was moved around the curved surface of the phantom. (b) 3D view of the 7 volumes showing the location of the reslice plane. (c) A blended view of the 7 reslices from the individual volumes. (d-g) From left to right: estimated diffuse back-scatter component d , estimated specular scattering strength t and estimated magnitude and direction of specular scattering.

angles and so can produce a large specular peak at a large angle that still satisfies the observations. Allowing n to vary improves the background. This may be because the extra flexibility can more easily fit the peak within the range of angles in which we have measurements available. Second, although the four-parameter exponential model has a better background than the Phong model, there are artifacts in the specular regions which are partly interpreted as diffuse scattering. Third, the four-parameter exponential model has a stronger specular component overall. Finally, a limitation of all methods is that at the end of each specular line, there is a bright feature in the diffuse image. This is because the ends of the lines are visible at any viewing angle and so are interpreted as diffuse scatterers. This also means that the ends of the lines in the directional image are reduced in magnitude compared to the centres.

The main purpose of this work is to distinguish diffuse and specular scattering in 3D data. Figures 4 and 5 show the results for our 3D simulated dataset. Both the 2D and 3D models were tested on 2D slices through the data. Figure 4 shows the axial-lateral slice and Fig. 5 shows the axial-elevational slice. In both figures it is clear that the 3D model has improved the separation of diffuse and specular components. In the 3D results, the background specular noise has been reduced as well as the artifact previously observed in the four-parameter 2D exponential model.

Figure 6 shows the 2D axial-lateral reslices in the 3D *in vitro* data taken approximately through the centre of the data. It is important that the images are not saturated, otherwise the models will not correctly fit to the observed intensity variation. In this case, the log-compression in creating the B-mode images was adjusted to avoid saturation of the specular line corresponding to the aluminium foil and hence the images appear darker in the background. Since the specular reflector is not completely flat, it can reflect strongly in more than one direction and so is visible at larger angles of incidence. For this reason the value of n calibrated in simulation is not accurate and we have not used the version of the algorithm with n fixed though we have used the same calibrated values to initialise the algorithms. The results show that the methods are able to distinguish diffuse and specular scattering to some extent since the specular line is visible in all cases. However, the 3D models have less of the specular line in the diffuse image and so are superior to the 2D.

4 Conclusions

We have presented several methods to visualise the diffuse and scattering components of tissue by imaging the tissue from multiple directions and observing the angular variation. This can be done either with a 2D or a 3D angular variation model. However, we have found that we get better results using a 3D model. Overall, the 3D exponential model gives a slightly better visual quality. In this paper, we have used a position sensor to register the images taken at different angles. A possible future development of this work is to record a single beam-steered image. This would fit in well with the 2D model which requires angular variation on a single plane. Alternatively, a 2D array transducer could produce a 3D steered image and so would not require a position sensor or image registration.

Acknowledgements

Umer Zeeshan Ijaz is supported by the UK Engineering and Physical Sciences Research Council (EPSRC) grant EP/F016476/1.

References

- [1] M. Vogt, J. Opretzka, and H. Ermert. Parametric imaging of specular reflections and diffuse scattering of tissue from multi-directional ultrasound echo signal data. In *Proceedings of the IEEE Ultrasonics Symposium*, pages 1963–1966, 2008.
- [2] R. F. Wagner, M. F. Insana, and D. G. Brown. Statistical properties of radio-frequency and envelope-detected signals with applications to medical ultrasound. *J. Opt. Soc. Am. A.*, 4(5):910–922, 1987.
- [3] G. Georgiou and F. S. Cohen. Statistical characterization of diffuse scattering in ultrasound images. *IEEE Transactions on Ultrasonics, Ferroelectrics, and Frequency Control*, 45(1):57–64, 1998.
- [4] T. Taxt. Separation of the diffuse, specular and quasiperiodic signal components in medical ultrasound images. In *Proceedings of the IEEE Ultrasonics Symposium*, volume 3, pages 1639–1644, 1994.

- [5] B. T. Phong. Illumination for computer generated pictures. *Communications of ACM*, 18(6):311–317, 1975.
- [6] J. H. Hokland and P. A. Kelly. Markov models for specular and diffuse scattering in restoration of medical ultrasound images. *IEEE Transactions on Ultrasonics, Ferroelectrics, and Frequency Control*, 43(4):660–669, 1996.
- [7] A. Gee, R. Prager, G. Treece, C. Cash, and L. Berman. Processing and visualizing three-dimensional ultrasound data. *The British Journal of Radiology*, 77:S186–S193, 2004.
- [8] J. J. Moré. The Levenberg-Marquardt algorithm: Implementation and theory. *Lecture Notes in Mathematics*, 630:105–116, 1978.
- [9] J. A. Jensen. Field: a program for simulating ultrasound systems. In *Proceedings of the 10th Nordic-Baltic Conference on Biomedical Imaging*, volume 4, pages 351–353, 1996.
- [10] R. W. Prager, A. H. Gee, and L. Berman. Stradx: real-time acquisition and visualization of freehand three-dimensional ultrasound. *Medical Image Analysis*, 3(2):129–140, 1999.
- [11] The Stradwin 3D ultrasound acquisition and visualisation system. <http://mi.eng.cam.ac.uk/~rwp/stradwin/>.
- [12] NDI: Accurate Measurement Solutions for Medical, Industrial, and Life Sciences Applications. <http://www.ndigital.com>.
- [13] G. M. Treece, A. H. Gee, R. W. Prager, C. J. C. Cash, and L. H. Berman. High-definition freehand 3-D ultrasound. *Ultrasound in Medicine and Biology*, 29(4):529–546, April 2003.